Bulletin of the Seismological Society of America, Vol. 106, No. 3, pp. 1002–1010, June 2016, doi: 10.1785/0120150181

Correlation of Wavefield-Separated Ocean-Generated Microseisms with North Atlantic Source Regions

by David Craig,* Christopher J. Bean,* Ivan Lokmer, and Martin Möllhoff*

Abstract Ocean-generated microseisms have the potential to be used as a proxy for ocean wave parameters. However, they are often comprised of contributions from multiple, coincidently active source regions. Using a seismic array, it should be possible to separate microseism data consisting of contributions from one or more source areas on the seafloor based on the wavenumber of the signals. Here we investigate the use of frequency–wavenumber filtering on data between 0.1 and 0.25 Hz, corresponding to double-frequency microseisms, recorded at the Eskdalemuir seismic array in Scotland. As the array is intended for shorter seismic wavelengths than those that occur at microseism frequencies, synthetic and scaled field experiments are performed to establish that the array geometry is suitable. Application is then made to microseism data from the array. Through a comparison with WAVEWATCH3 numerical ocean wave data, we demonstrate that the frequency–wavenumber (f-k) filter enables the separation of microseisms into its different geographical source components. This separated microseism data give proxy access to local sea state conditions that are masked in the total microseism wavefield.

Introduction

Oceans generate persistent low-frequency background seismic signals known as microseisms through a mechanical coupling with the Earth's crust. The microseism spectrum generally consists of two peaks. The longer period (∼10–20 s) low-amplitude signals are known as primary frequency microseisms (PFM) and are the result of pressure fluctuations on an undulating seafloor beneath wind-generated ocean surface gravity waves (Hasselmann, 1963). These pressure fluctuations decrease exponentially with depth, limiting PFM generation to shallow water regions. The resulting microseisms have periods approximately equal to those of the causative ocean gravity waves.

The shorter period peak (∼3–10 s) dominates the microseism spectrum and indicates secondary or double-frequency microseisms (DFM). DFM are a consequence of pressure fluctuations on the seafloor beneath standing ocean gravity waves. These standing waves are the superposition of oppositely traveling ocean wavetrains with similar spectral characteristics (Longuet-Higgins, 1950). The frequency of the resulting microseisms is twice the frequency of the formative traveling waves. DFM sources are not limited to shallow water regions as the causative ocean wave pressure fluctuations are independent of depth.

More recently, Ardhuin *et al.* (2011) advanced the understanding of the controls on microseism generation, highlighting the importance of the ocean wave directional spectrum. For the near-coastal DFM spectrum, it is likely that coastal reflections play an important role in creating the necessary wave–wave interactions (Bromirski and Duennebier, 2002; Ardhuin *et al.*, 2011). However, more distant sources may contribute at times, with the relative contributions of each being the subject of some debate (Obrebski *et al.*, 2012; Bromirski *et al.*, 2013). Surface wave propagation effects at the ocean–continent boundary have been offered as a possible explanation. However, this is also debated (Ying *et al.*, 2014; Gualtieri *et al.*, 2015).

The relationship between ocean-generated microseisms and the local ocean wavefield allows microseism time series to be used as a proxy for ocean wave characteristics, as seen on ocean buoys (Bromirski *et al.*, 1999; Donne *et al.*, 2014). However, for the proxy to be valid, the microseism data must relate to a source area at or near an ocean buoy. In the northeast Atlantic, variability in the local ocean wavefield means that time series recorded at near coastal seismic stations can consist of contributions from different coincidently active source locations (Moni *et al.*, 2013; Beucler *et al.*, 2015). A single region may dominate at any one time or multiple regions can contribute simultaneously. Because the microseism sources are continuous, it is reasonable to assume that each source region generally contributes to some extent, although the temporal variations in the relative contributions from each source region are considerable. This means that to obtain ocean wave characteristics from microseism time series, some form of wavefield separation would be of benefit.

*Now at Dublin Institute of Advanced Studies, Geophysics section, Dublin, Ireland.

Seismic arrays consist of multiple sensors (or array elements) distributed in space in such a way as to provide improved information on the seismic wavefield. Arrays are extremely useful tools allowing significant increases in signal-to-noise ratio as well as information on the propagation direction and phase of signals recorded by the array. Array methods combine the signal from each array element in such a manner as to emphasize the portion of the signal that is coherent across the array and suppress everything else. The dependence on coherency imposes significant restraints on the array geometry.

An important quantity that can be obtained through array analysis is the frequency–wavenumber (f-k) spectrum, which is an image of the energy density as a function of f and k. For directional studies, the f-k spectrum provides an efficient method to calculate beampower depending on direction and phase speed (Rost and Thomas, 2002). In exploration studies, it is commonly used to remove coherent noise from signals (Yilmaz, 2001). For example, different wave types are separable in f-k space based on the difference in their apparent velocities.

Many different methods exist for calculating the f-k spectrum. In exploration seismology, the discrete Fourier transform (DFT) is often used. However, this puts an extra constraint on the array geometry in that uniform spacing is required. The arrays used then tend to be straight lines or rectangular planes. The DFT is simply applied to each dimension of a data matrix for which columns are the signal data recorded at each array element. Similarly, the inverse transform can be applied to recover the individual waveforms or a beam. Uniform arrays are not common in directional-based studies and processing methods differ for nonuniform arrays. The f-k spectrum is calculated by covariance analysis (Kirlin and Done, 1999) of the data matrix in the temporal–frequency domain. This, however, does not provide the phase information required for the inverse transform and, as such, is not suitable for filtering in the f-k domain.

Because microseisms are largely composed of surface waves (Tanimoto *et al.*, 2006), velocities of signals from different source areas measured at an array can be expected to be similar. However, if one considers plane waves crossing a linear array with different propagation directions, they will have different apparent velocities and, as such, should be separable in f-k space. As signals with different apparent velocities will occupy different regions of f-k space, it is possible to separate them in that domain and then apply an inverse transform to obtain time-series data related to a single source component. The previously discussed conventional methods of spectral estimation, which have an inverse transform, require uniform spacing of receivers in the array. This requires the geometry of the array to be either a rectangular grid or a line. As a grid would require a large number of receivers, the use of a linear array for f-k filtering is investigated here.

To that end f-k wavefield separation is applied to microseism data recorded on each linear branch from the Eskdalemuir array (EKA) in Scotland; see Figure 1a,b for the array location and geometry. As the EKA lines have a small aperture (~8 km) relative to microseism wavelengths, we expect the resolution to be poor. Hence, a filter is designed that has a wide passband to allow for the imprecise knowledge of the wavenumber spectrum.

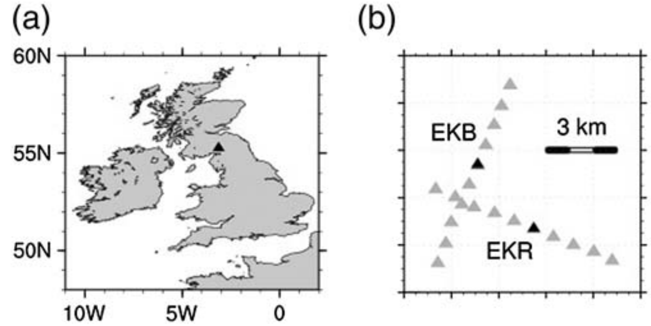

Figure 1. (a) The location and (b) geometry of the small aperture array at Eskdalemuir array (EKA) Scotland. The center stations for each array line (EKB5 and EKR5) are marked in black.

To evaluate the effectiveness of such a filter, we start by describing the data used in the next section, followed by a section describing the spatial relationship between DFM recorded at EKA and the ocean wavefield. In the next section, the design of an f-k filter for a small-scale array is considered and then tested using synthetic data and a down-scaled field experiment replicating the EKA geometry. In the penultimate section, the filter is applied to EKA data recorded over a period of one month. The final section discusses the separation procedure and source locations observed using the separated data.

Data

This study includes the use of synthetic seismograms, geophone records for small scale experiments, broadband seismometer records collected from EKA during April 2012, and global model ocean wave heights (WAVEWATCH III [WW3]) from the same period.

Synthetic seismograms are generated using the reflectivity method (Kennett, 1985). A velocity model representative of the crust in the area of study was adopted from Hauser *et al.* (2008). The seismic source used in the simulations was an impulsive vertical force located just below the free surface. The resulting data were then convolved with a microseism displacement sample recorded in Ireland, which had been low-pass filtered below 0.5 Hz. Synthetic microseism data comprising multiple spatially distributed sources were acquired through linear combinations of such data vectors.

A scaled field experiment was conducted using a 9 m line of 10 equally spaced geophones. The source was a sledge hammer impacted on a metallic plate. Signals were generated individually for multiple source locations and then summed at each geophone location. This allows a comparison to be made between the original signal and the separated one.

Significant wave height (SWH) data from the WW3 model with parameterizations by Ardhuin *et al.* (2010) were obtained from the wave hindcast database, which is available

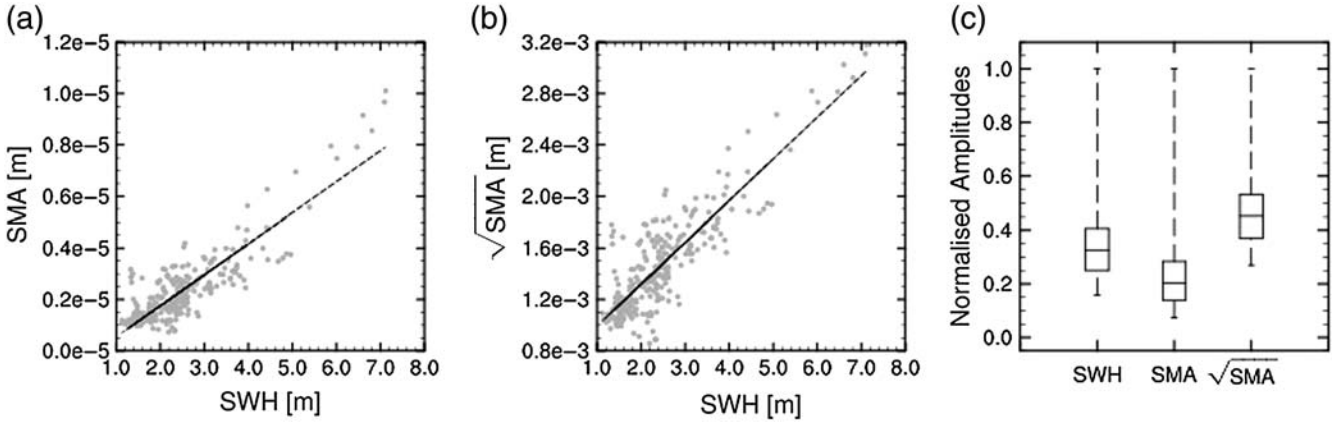

Figure 2. (a) Scatter plot for significant microseism amplitude (SMA) for April 2012 recorded at EKB5 against WAVEWATCH III (WW3) significant wave height (SWH) for the same time period. SWH relates to point of maximum correlation between SMA and model ocean wave heights in WW3 model domain (54°, 10.5°). Linear regression line is shown in black. (b) Scatter plot for $\sqrt{\text{SMA}}$ against SWH. Using $\sqrt{\text{SMA}}$ has helped to linearize the relationship. (c) Boxplots for SWH, SMA, and $\sqrt{\text{SMA}}$. The box shows the range of data falling between the 25th and 75th percentiles, the horizontal line inside the box shows the median value, and the whiskers (dotted lines) show the complete range of the data. Each quantity shows positive skew. The data for the boxplots have been normalized between 0 and 1 for display purposes.

through the IOWAGA project. This provides SWH over a global grid with 0.5° spacing on a 3-hour time step. SWH is the convention for describing measured and model ocean wave heights. It is defined as four times the standard deviation of the surface elevation. For WW3, this is calculated from wave spectral density $S(k, \theta)$.

$$E = \int S(k, \theta) dk d\theta, \tag{1}$$

$$\text{SWH} = 4\sqrt{E}. \tag{2}$$

Seismic data were obtained from AWE Blacknest for the Eskdalemuir broadband seismic array. Time series from EKA were used to calculate a significant microseism amplitude (SMA), similar to the quantity used by Essen *et al.* (2003), for comparison with the SWH statistic from the ocean model data. To calculate this quantity, a 1200 s displacement time series, sampled at 1 Hz, was cut from the data and subdivided into 11,200 s overlapping windows. The spectral density is then calculated for each subwindow and the results averaged to provide the total spectral density estimate. This is then used to calculate SMA in the same manner as SWH for frequencies between 0.1 and 0.25 Hz.

Relationship between Microseism Amplitudes and the Model Ocean Wavefield

As DFM are the result of ocean wave activity, we expect DFM amplitude time series to correlate well with ocean wave time series at or near the source region generating the microseisms. Previous studies have used Pearson's product-moment correlation coefficient to quantify the relationship between microseisms and model ocean wave heights (Essen *et al.*, 1999, 2003). For Pearson's method to accurately describe the correlation between two variables, certain assumptions have to be made about the data. Specifically, the data should share a linear relationship, there should be no significant outliers, and the variables should be approximately normally distributed (see Kowalski, 1972, for a discussion on the effects of nonnormality). Essen *et al.* (1999) showed that when correlating model SWH, larger correlation coefficients could be obtained if SWH is correlated with $\sqrt{\text{SMA}}$ rather than with SMA. Although this result is consistent with DFM being proportional to the square of the seafloor pressure (Longuet-Higgins, 1950), it does not allow for any nonnormality in the distribution of SWH. Data recorded on station EKB5 for the month of April 2012 are compared with WW3 SWH in Figure 2. The scatter plots for both SMA against SWH and $\sqrt{\text{SMA}}$ against SWH show that using $\sqrt{\text{SMA}}$ is clearly an effective way of linearizing the relationship between the variables. Because of the large difference between SWH and SMA values, the data for the boxplots have been normalized between 0 and 1. Each variable shows positive skew violating the assumption of a normal distribution for Pearson's method. To test the effects of the nonnormal distribution, we compare results from Pearson's method with results from Spearman's rank-order correlation coefficient. Spearman's method is calculated as follows:

$$\rho = 1 - \frac{6 \sum d_i^2}{n(n^2 - 1)}, \tag{3}$$

in which d_i is the difference in paired ranks and n is the number of cases. The only assumption is that there is a monotonic relationship between the variables. The advantage is that as Spearman's method is nonparametric it should not be affected by the skewed data.

Figure 3 shows the correlation results between model wave heights and microseisms for both methods. The maps in Figure 3a,b are created by correlating DFM data from station EKB5 for the month of April 2012 with SWH time series for each node in the WW3 model domain. This gives a correlation

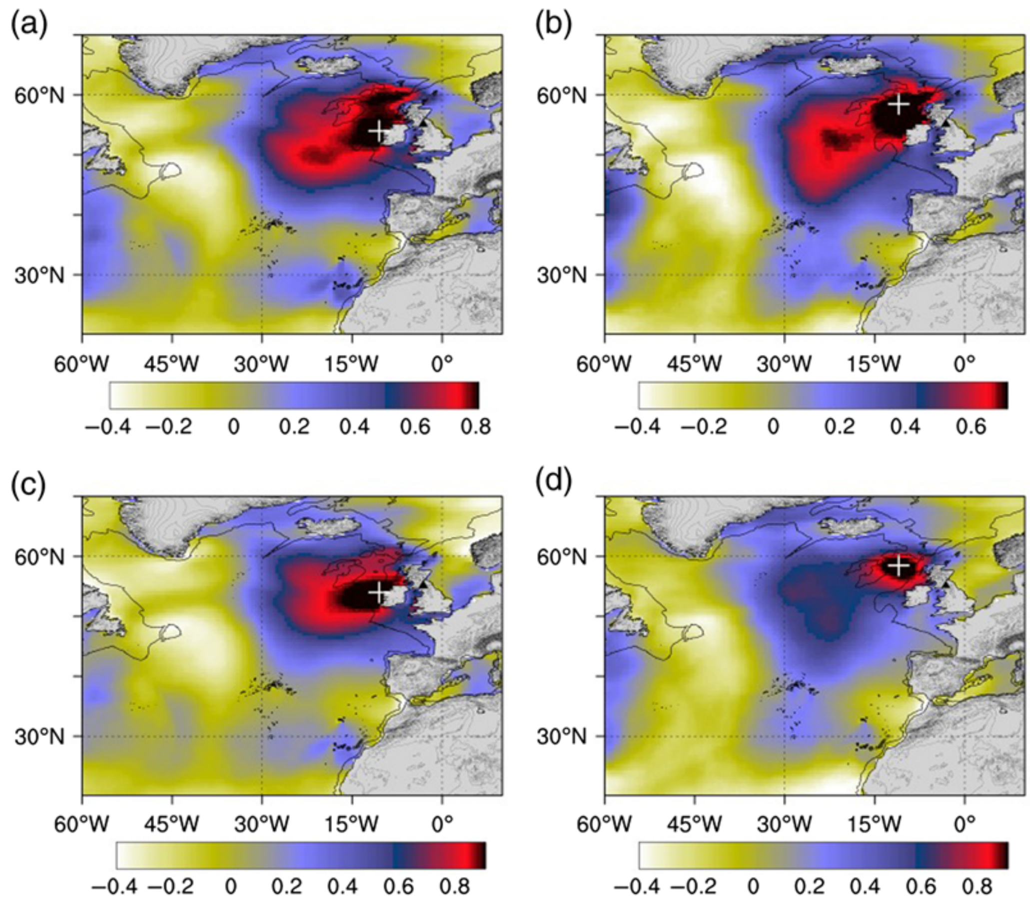

Figure 3. (a) Map of Pearson's correlation coefficients for WW3 SWH and EKB5 $\sqrt{\text{SMA}}$ for April 2012. (b) Map of Spearman's correlation coefficients for WW3 SWH and EKB5 SMA for April 2012. (c) Spatial autocorrelation map for ocean wave model data relative to the point of maximum correlation according to Pearson's method. (d) Autocorrelation map for ocean wave model data relative to the point of maximum correlation according to Spearman's method. The 1-km-depth contour is shown in black and the triangle marks the approximate location of EKA. The color version of this figure is available only in the electronic edition.

coefficient for every point in the model domain. Figure 3a was generated using Pearson's method with $\sqrt{\text{SMA}}$ and Figure 3b was generated using Spearman's method with SMA (because the data are ranked for Spearman's method there is no advantage in using $\sqrt{\text{SMA}}$). Both methods show a high degree of correlation in the northeast Atlantic close to the seismic array. However, for Pearson's method the maximum occurs off the northwest coast of Ireland and for Spearman's method it occurs further to the north. Strong correlations also appear in other regions; for example, a positive anomaly can also be seen on the western side of the Atlantic. Negative coefficients are also present. As there is no physical basis for negative correlation between SMA and SWH, this can be interpreted as a measure of the degree to which correlation does not imply causality. To understand the significance of the local extrema, the SWH time series from the point where the maximum correlation coefficient occurred was also correlated with the SWH model data for every spatial point in the model (Fig. 3c,d). The resulting maps demonstrate the degree of spatial autocorrelation within the model data. For the Pearson's coefficient map, the related spatial autocorrelation map (Fig. 3c) is very similar to the microseism correlation map (Fig. 3a) with extrema appearing in the same locations. The coincidence of the local extrema means it is difficult to interpret them as source areas, as they can be explained by the spatial autocorrelation within the SWH data (although there is nothing to prevent a source occurring in a region with high autocorrelation). When comparing the Spearman's coefficient map to the related spatial autocorrelation map (Fig. 3b,d), the overall shape is again similar with the spatial autocorrelation map having a more peaked appearance.

Because of the violation of the assumptions for Pearson's method and the degree of spatial autocorrelation within the data, in the following sections we limit the discussion to the global maximum of the Spearman correlation coefficients.

f-k Filtering of Microseism Data on a Small-Scale Linear Array

In the previous section, it was shown that spatial autocorrelation in the model SWH prevented local maxima in maps of the correlation coefficients for SWH and SMA being interpreted as source areas. Because this is a limitation of the method and does not preclude the existence of other source areas, a filter is designed to separate the microseism wave-

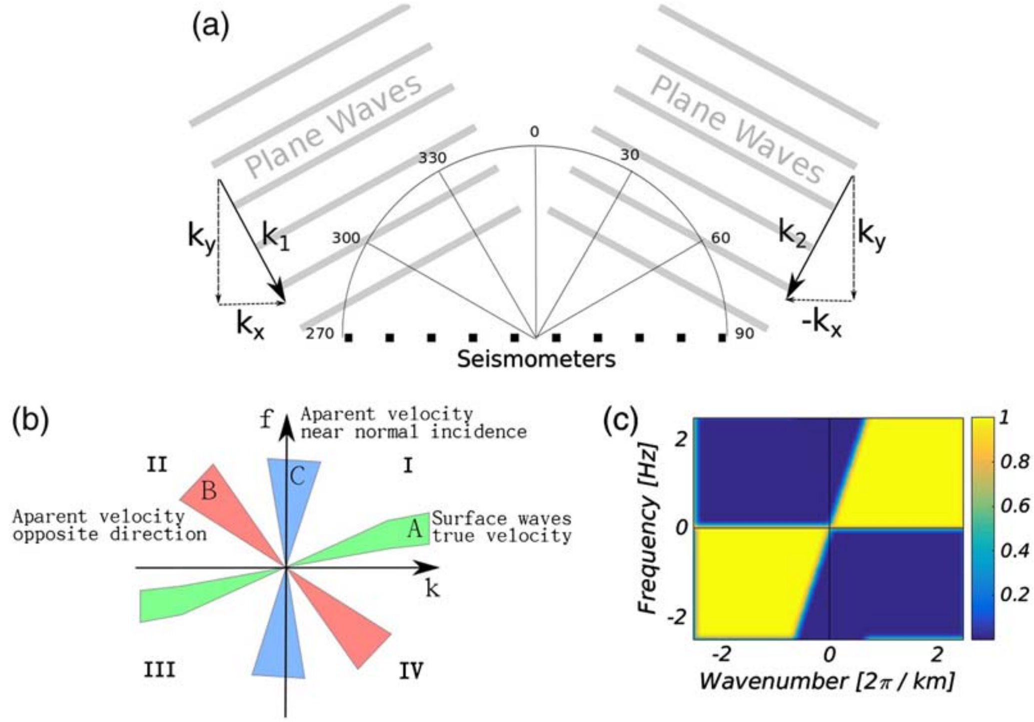

Figure 4. (a) Illustration of plane waves from two different source regions crossing a linear array of seismometers. (b) Representation of signals in f-k domain. Signal A represents true velocity for surface waves and shows dispersion associated with a hypothetical subsurface velocity gradient. Signal B represents the apparent velocity of a signal traveling across the array where the component of the wavenumber along the array has the opposite sign to signal A (see above). Signal C represents the signal existing on both sides of the spectrum for a signal traveling on a path almost normal to the array. (c) Response of the filter in f-k domain. The color version of this figure is available only in the electronic edition.

field into different source components based on propagation direction.

Filter Design

The 2D Fourier transform is a linear operation that decomposes multichannel data into its frequency (f) and wavenumber (k) components. The resulting spectrum is an image of the energy density as a function of f and k (f-k spectrum). For a time–space domain signal $w(x,t)$, the transform is

$$W(f,k) = \frac{1}{2\pi}\int_{-\infty}^{\infty}\int_{-\infty}^{\infty} w(x,t)\exp(-i2\pi(ft-kx))dxdt. \quad (4)$$

This allows different wave phenomena to be separated and filtered based on differences in apparent velocity (Yilmaz, 2001; Strobbia, 2003). Typically the transform is carried out using the fast Fourier transform. This introduces a constraint on data acquisition in that the traces are required to be uniformly spaced.

Signals crossing a linear array (Fig. 4a) will show differences in apparent velocity dependent on the direction of propagation. This should allow them to be separated in the f-k domain. In practice, the separation of the data is limited by the following factors:

1. In the f-k domain, the spectrum of a propagating wavefield is necessarily confined to a conical region that extends radially from the origin (Fig. 4b). For a wavefield with multiple coherent signals, convergence of the signals toward the origin means they may become superposed. The array resolution affects the width of the conical region. For signals with similar wavenumbers, a high degree of resolution is required, meaning the array aperture needs to be greater than the wavelength of interest.
2. To prevent spectral leakage, the data are normally tapered in the spatial dimension. Because of the uncertainty principle this results in a decrease in resolution of k.
3. Signals traveling along a path not parallel to the array will have a larger apparent wavelength, which effectively reduces the resolution of the array.

If one considers two signals simultaneously crossing a linear array with the components traveling parallel to the array moving in opposite directions, the wavenumbers on such signals will have opposite signs and hence appear in opposing regions of f-k space. The time domain representation of such signals is illustrated in Figure 4a. In the f-k domain (Fig. 4b), the energy density of a signal with a positive wavenumber appears in quadrants I and III and the energy for a signal with a negative wavenumber appears in quadrants II and IV. Signals traveling on a path (near-)normal to the array will have energy on both sides of the spectrum. With these ideas in mind, it is possible to design a 2D finite impulse response (FIR) filter that will suppress signals with a velocity component parallel to the array based on the sign of the

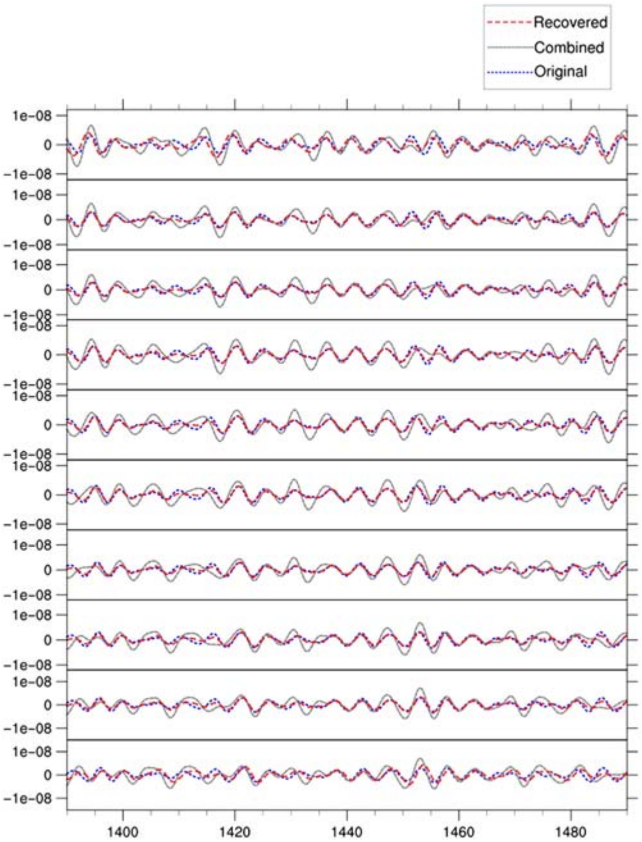

Figure 5. Synthetic waveforms for each receiver for signals with back azimuths of 45° and 315°. The original signal relates to a signal crossing the array with a 45° back azimuth. The combined signal corresponds to the linear sum of two signals with back azimuths of 45° and 315°. The separated signal relates to the signal with back azimuths of 45° recovered after *f-k* filtering. The color version of this figure is available only in the electronic edition.

wavenumber, or more intuitively its direction along the array, and also limit the amount of energy from signals traveling normal to the array.

Such a filter was designed using the window method, by defining the desired response in the *f-k* domain and applying the inverse 2D Fourier transform to get the time–space domain representation. This is multiplied by a suitable window function (2D Gaussian) to obtain the FIR coefficients. As the impulse response and the window used were both symmetrical with respect to the origin, the resulting filter is zero phase (Lim, 1990). The *f-k* response of such a filter is shown in Figure 4c; in this case it will suppress energy in quadrants I and III. The aforementioned filter does not consider individual signals but instead suppresses all energy from one end of the array.

Synthetic Tests

To determine if such an *f-k* filter would be effective for linear arrays with the same geometry as the EKA lines, some synthetic tests were performed. Synthetic signals for two sources crossing a 10-station linear array with an aperture of 8 km (approximate dimensions of the array lines in EKA) were

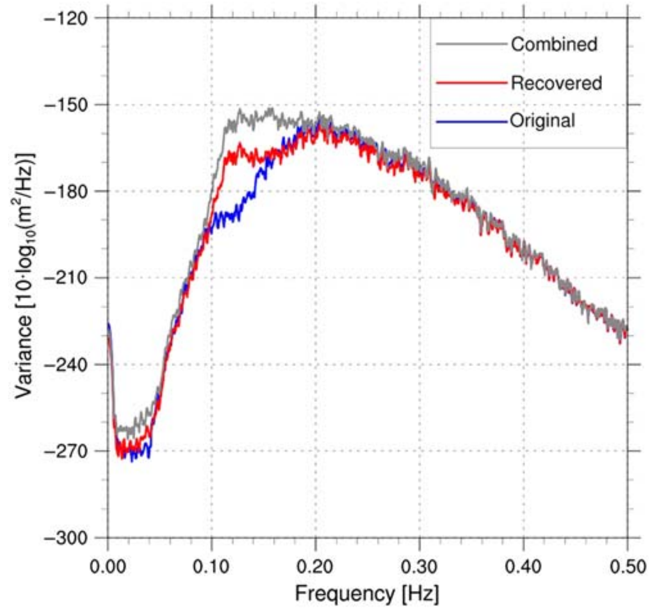

Figure 6. Variance spectra for the central receiver shown in Figure 5. The color version of this figure is available only in the electronic edition.

generated as described in the data section. A 10% cosine taper was applied to each trace. No spatial tapering was applied as it further reduces the resolution of the array. Some energy was lost due to spectral leakage, but it was not a significant amount due to the wide passband on the filter. The signals had back azimuths of approximately 45° and 315° in the coordinate system shown in Figure 4a.

Figure 5 shows a comparison of the original 45° waveforms with the linear combination of both waveforms and the separated waveforms after the wavefield associated with the 315° source was suppressed in *f-k* space.

Figure 6 shows a comparison of the variance spectra for each signal on the center receiver in the array. The signal is well recovered above ~0.15 Hz, below that not all energy from the interference signal is suppressed, but it is significantly reduced.

Scaled Experiment

To determine if similar results could be obtained with physical data, a scaled field test was performed with known source locations. Seismograms from a line of geophones were generated, as described in the data section, for sources along back azimuths of 45° and 315° in the array coordinate system (Fig. 4a).

For the geometry to be comparable with the EKA lines, the experiment needed to be scaled accordingly. The Eskdalemuir lines consist of 10 equally spaced receivers and are ~8 km long. Microseism wavelengths at 5 s are ~15 km, so for a 9 m line of 10 equally spaced geophones, wavelengths of ~20 m are required. Surface wave velocity at the test site was ~600 m/s; hence frequencies near 30 Hz were required. To facilitate this, the seismograms were filtered between

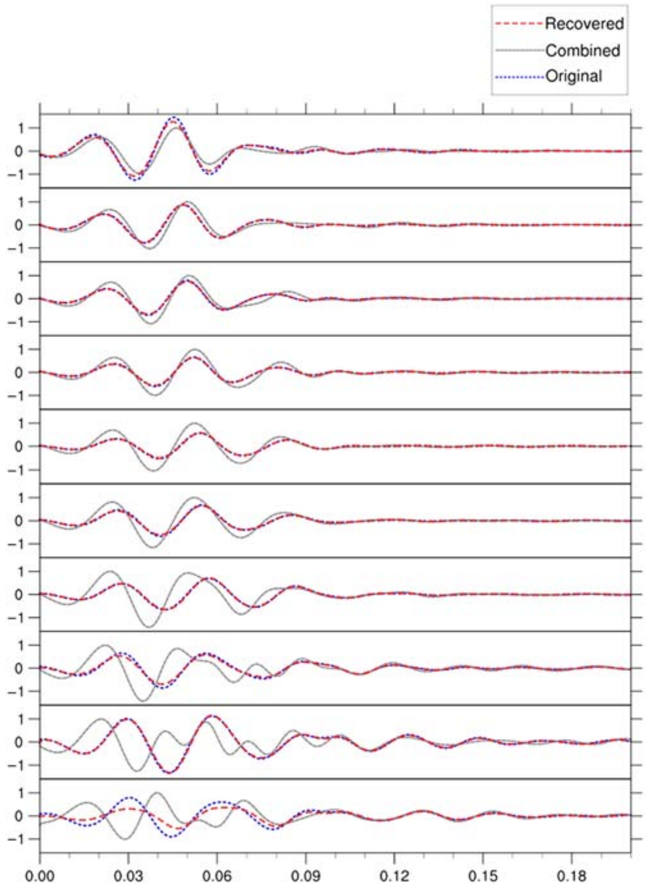

Figure 7. Geophone waveforms for signals with back azimuths of 45° and 315°. The original signal relates to a signal crossing the array with a 45° back azimuth. The combined signal corresponds to the linear sum of two signals with back azimuths of 45° and 315°. The separated signal relates to the signal with back azimuths of 45° recovered after f-k filtering. The color version of this figure is available only in the electronic edition.

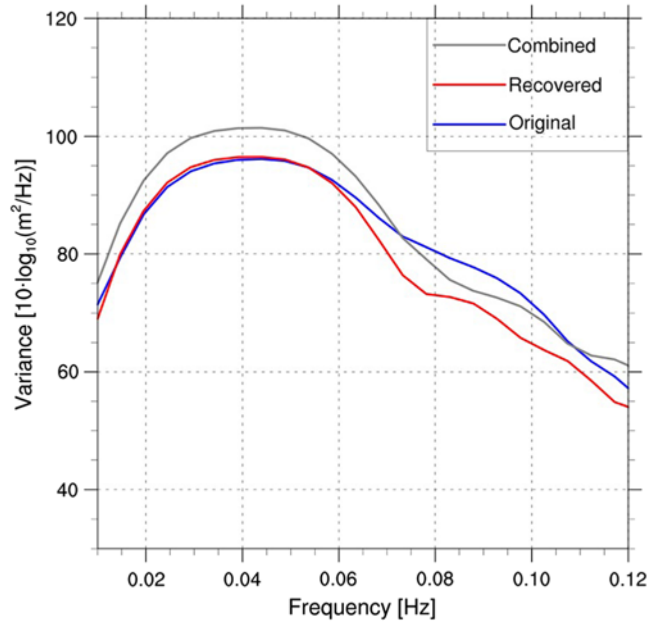

Figure 8. Variance spectra for the central receiver shown in Figure 7. The color version of this figure is available only in the electronic edition.

20 and 40 Hz before being combined. The separation procedure was then applied to the data. Figure 7 shows the waveforms for the data, where we have recovered the waveform for the 45° source. Figure 8 compares the variance spectra for the waveforms on the central array receiver. The spectrum is very well recovered across the frequencies of interest in this case. As the signal was successfully separated in this scaled field experiment, it encouraged us to apply the scheme to microseism data from EKA.

Application of the f-k Filter to Microseism Array Data

To evaluate the effectiveness of the wavefield separation procedure described in the previous section, physical microseism data recorded at EKA were separated and compared with ocean wave model data. The array consists of two straight lines of 10 equispaced instruments intersecting at right angles (Fig. 1b). The lines are orientated approximately south-southwest to north-northeast (EKB) and west-northwest to east-southeast (EKR).

Because a comparison of the original source and the separated waveforms as carried out in the previous sections was not possible for the EKA data, the degree of correlation between the separated data and the model ocean wavefield was assessed to give some indication of the performance of the separation procedure.

For comparison with the model SWH data, the separation procedure was applied to both lines in the array for a 1200 s window at the end of every third hour for the month of April 2012. The f-k filter was applied to recover signals from either end of each of the array lines and SMA calculated for a receiver at the center of each (EKB5 and EKR5, Fig. 1b). This yields four time series, which should be related to energy from different regions of the ocean wavefield. The correlation coefficients were then calculated for each of the separated microseism amplitudes and the model ocean wave heights. Figure 9 shows the maps of the correlation coefficients for each time series. The region highlighted in each figure represents the area to which we expect the filtered data to be sensitive. Figure 9a has a maximum coefficient of 0.84 off the southwest coast of Ireland, which is consistent with the signal coming from the south-southwest. In Figure 9b, we expect the data to be sensitive to signal with a component from the north-northeast and, correspondingly, the maximum of 0.74 shifts to an area off the northwest coast of Scotland. Figure 9c shows that the maximum of 0.79 occurs off the north coast of Ireland. This is very similar to the unseparated data (Fig. 3f) suggesting that the majority of the signal is contained in the passband for this filter. Finally, in Figure 9d, we expect the data to be sensitive to signal from the east-southeast and although coefficients in the western portion of the map are strongly reduced, the maximum of 0.68 occurs to

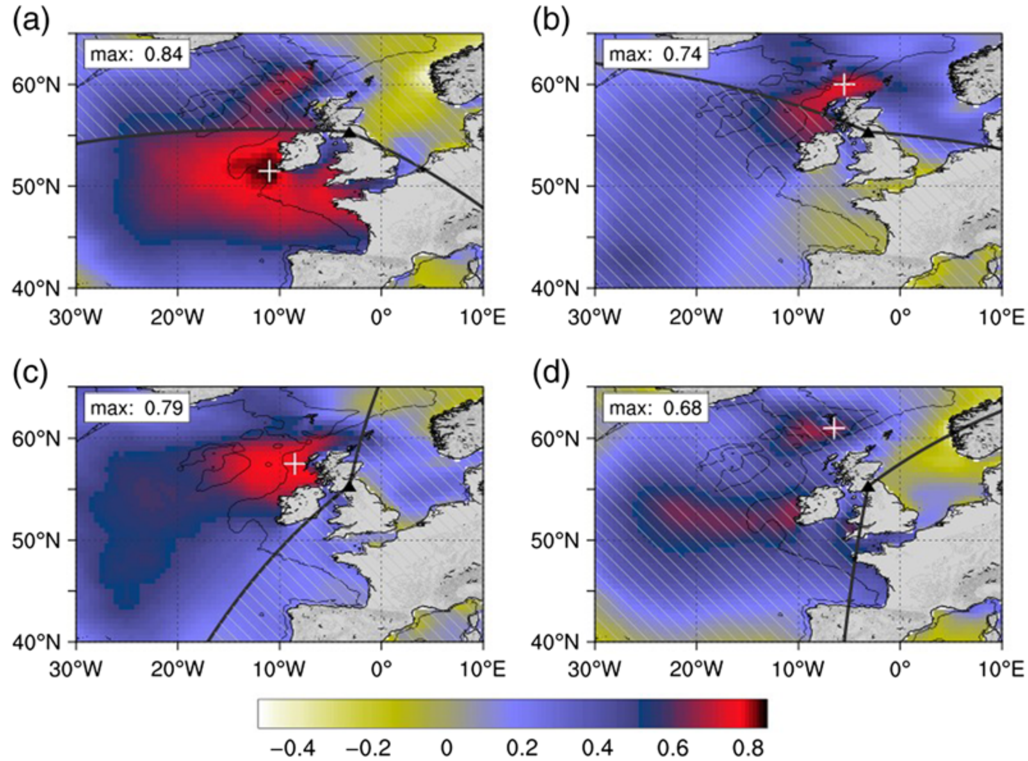

Figure 9. Spearman's correlation coefficients for f-k filtered data. Coefficients relate to SMA for EKB5 and EKR5 correlated with SWH. The black triangle shows the location of the array line where the f-k filter was applied (not to scale). The $\pm 75°$ limits for each application of the filter are indicated by the black lines radiating from the array. The approximate region excluded by the filter is indicated by the gray hatching. The 1-km-depth contour is shown by the black contour and the white cross shows the position of the global maximum. (a) Coefficients for EKB5 f-k filtered to suppress signal with a velocity component from the north-northeast. (b) Coefficients for EKB5 f-k filtered to suppress signal with a velocity component from the south-southwest. (c) Coefficients for EKR5 f-k filtered to suppress signal with a velocity component from the east-southeast. (d) Coefficients for EKR5 f-k filtered to suppress signal with a velocity component from the west-northwest. The color version of this figure is available only in the electronic edition.

the northwest of Scotland and no significant values are seen in the eastern portion of the map. We interpret this as sources in the North Sea (if any are active) not making a significant contribution to SMA recorded at EKA during the analysis period. The maximum occurs on the west side of the array, which is most likely explained by the energy on a path close to normal with the array that spreads onto the opposite side of the f-k spectrum due to the low resolution of the array.

Discussion and Conclusions

The relationship between microseisms and ocean waves allows seismic data to be used as a proxy for ocean wave parameters (Bromirski *et al.*, 1999; Aster *et al.*, 2010). Correlation of microseism time series with the model ocean wavefield can provide information on the microseism source regions. However, it was shown that this can be misleading if an appropriate correlation method is not used. Pearson's correlation coefficient can give erroneous results if the data are skewed. We suggest a nonparametric method such as Spearman's rank-order correlation, but it may also be possible to use Pearson's method if outliers are first removed and an appropriate transform applied to allow for the nonnormality of the data.

Considering the total microseism wavefield as consisting of contributions from several independent source areas, each of which is a potential proxy for ocean wave properties in that region, we find it beneficial to apply an f-k filter to separate the microseism wavefield into components related to each source area. We designed a filter to apply this methodology to data from an array at Eskdalemuir, Scotland. Because the array is relatively small compared with microseism wavelengths, we first showed that the approach was viable by performing synthetic and scaled-field experiments.

Although the resolution of EKA is not ideal for studying microseisms, application of the f-k filter before correlation with the ocean wavefield revealed at least two regions that contribute to SMA recorded at EKA in the study period that could not be explained by autocorrelation in the ocean wavefield. This suggests the filter is effective and can provide independent time-series data for each source region. Microseism amplitudes obtained through application of the f-k filter correlated well with SWH in specific regions of the ocean wavefield. If energy traveling with a velocity component from one end of the array is suppressed, the correlation coefficients off that end of the array are also reduced. This implies that the time series have been modified in a sensible way, consistent with how we expect the filter to modify the wavefield. The largest correlation coefficients occur in regions within the continental shelf from the southwest of Ireland to the north of Scotland. However, the correlation between the SWH and SMA time series is likely more sensitive to the spatially stable sources expected from coastal reflections. That is, it would not highlight more transient sources such as those beneath rapidly moving storms. As such, contributions from storms over pelagic regions cannot be ruled out. Coastal reflections are thought to play a significant role in DFM generation, particularly on western ocean margins such as the study area (Bromirski and Duennebier, 2002; Ardhuin *et al.*, 2011). As such, the highlighted source areas likely correspond to the dominant source areas for the analysis period.

Sources in the identified areas have been reported before (Friedrich *et al.*, 1998; Chevrot *et al.*, 2007; Moni *et al.*, 2013). However, here we implemented a method that provides time series related to geographically separated yet time-coincident microseism source areas. The ability to separate the wavefield in this manner could potentially be used to quantify local ocean wave parameters for separate regions.

Data and Resources

Array data used in this work were provided by AWE Blacknest. Model significant wave heights (SWHs) from WAVEWATCH III (WW3) were obtained from the Ifremer IOWAGA FTP site.

Acknowledgments

We would like to thank the two anonymous reviewers whose comments helped to improve this article. This work was supported by the Science Foundation Ireland Principal Investigator Award through the Wave-Obs Project 10/IN.1/1301. We would like to thank Louis De Barros for the reflectivity code and to acknowledge the Obspy software library, which was used in this study.

References

Ardhuin, F., E. Rogers, A. V. Babanin, J.-F. Filipot, R. Magne, A. Roland, A. van der Westhuysen, P. Queffeulou, J.-M. Lefevre, L. Aouf, *et al.* (2010). Semi-empirical dissipation source functions for ocean waves. Part I: Definition, calibration, and validation, *J. Phys. Oceanogr.* **40,** no. 9, 1917–1941.

Ardhuin, F., E. Stutzmann, M. Schimmel, and A. Mangeney (2011). Ocean wave sources of seismic noise, *J. Geophys. Res.* **116,** C09004, doi: 10.1029/2011JC006952.

Aster, R. C., D. E. McNamara, and P. D. Bromirski (2010). Global trends in extremal microseism intensity, *Geophys. Res. Lett.* **37,** no. 14, L14303, doi: 10.1029/2010GL043472.

Beucler, E., A. Mocquet, M. Schimmel, S. Chevrot, O. Quillard, J. Vergne, and M. Sylvander (2015). Observation of deep water microseisms in the North Atlantic Ocean using tide modulations, *Geophys. Res. Lett.* **42,** no. 2, 316–322, doi: 10.1002/2014GL062347.

Bromirski, P. D., and F. K. Duennebier (2002). The near-coastal microseism spectrum: Spatial and temporal wave climate relationships, *J. Geophys. Res.* **107,** no. B8, ESE 5-1–ESE 5-20.

Bromirski, P. D., R. E. Flick, and N. Graham (1999). Ocean wave height determined from inland seismometer data: Implications for investigating wave climate changes in the NE Pacific, *J. Geophys. Res.* **104,** no. C9, 20,753–20,766.

Bromirski, P. D., R. A. Stephen, and P. Gerstoft (2013). Are deep-ocean-generated surface-wave microseisms observed on land? *J. Geophys. Res.* **118,** no. 7, 3610–3629.

Chevrot, S., M. Sylvander, S. Benahmed, C. Ponsolles, J. M. Lefèvre, and D. Paradis (2007). Source locations of secondary microseisms in Western Europe: Evidence for both coastal and pelagic sources, *J. Geophys. Res.* **112,** no. B11301, doi: 10.1029/2007JB005059.

Donne, S., M. Nicolau, C. Bean, and M. O'Neill (2014). Wave height quantification using land based seismic data with grammatical evolution, *2014 IEEE Congress on Evolutionary Computation (CEC)*, Beijing, 6–11 July 2014, 2909–2916, doi: 10.1109/CEC.2014.6900563.

Essen, H.-H., J. Klussmann, R. Herber, and I. Grevemeyer (1999). Does microseisms in Hamburg (Germany) reflect the wave climate in the North Atlantic? *Deutsche Hydrographische Zeitschrift* **51,** no. 1, 33.

Essen, H.-H., F. Krüger, T. Dahm, and I. Grevemeyer (2003). On the generation of secondary microseisms observed in northern and central Europe, *J. Geophys. Res.* **108,** no. B10, 2506+.

Friedrich, A., F. Krüger, and K. Klinge (1998). Ocean-generated microseismic noise located with the gräfenberg array, *J. Seismol.* **2,** no. 1, 47–64.

Gualtieri, L., E. Stutzmann, Y. Capdeville, V. Farra, A. Mangeney, and A. Morelli (2015). On the shaping factors of the secondary microseismic wavefield, *J. Geophys. Res.* **120,** no. 9, 6241–6262.

Hasselmann, K. (1963). A statistical analysis of the generation of microseisms, *Rev. Geophys.* **1,** no. 2, 177–210.

Hauser, F., B. M. O'Reilly, P. W. Readman, J. S. Daly, and R. Van den Berg (2008). Constraints on crustal structure and composition within a continental suture zone in the Irish Caledonides from shear wave wide-angle reflection data and lower crustal xenoliths, *Geophys. J. Int.* **175,** no. 3, 1254–1272.

Kennett, B. L. N. (1985). *Seismic Wave Propagation in Stratified Media, Cambridge Monographs on Mechanics*, Cambridge University Press, London, United Kingdom.

Kirlin, R. L., and W. J. Done (1999). *Covariance Analysis for Seismic Signal Processing*, Geophysical Development series, Vol. 8, Society of Exploration Geophysicists, Tulsa, Oklahoma.

Kowalski, C. J. (1972). On the effects of non-normality on the distribution of the sample product-moment correlation coefficient, *Appl. Stat.* **21,** no. 1, 1–12.

Lim, J. S. (1990). *Two-Dimensional Signal and Image Processing*, Prentice Hall, Inc., Upper Saddle River, New Jersey.

Longuet-Higgins, M. S. (1950). A theory of the origin of microseisms. Philosophical transactions of the royal society of London A: Mathematical, *Phys. Eng. Sci.* **243,** no. 857, 1–35.

Moni, A., D. Craig, and C. J. Bean (2013). Separation and location of microseism sources, *Geophys. Res. Lett.* **40,** no. 12, 3118–3122.

Obrebski, M. J., F. Ardhuin, E. Stutzmann, and M. Schimmel (2012). How moderate sea states can generate loud seismic noise in the deep ocean, *Geophys. Res. Lett.* **39,** no. 11, doi: 10.1029/2012GL051896.

Rost, S., and C. Thomas (2002). Array seismology: Methods and applications, *Rev. Geophys.* **40,** no. 3, 1008, doi: 10.1029/2000RG000100.

Strobbia, C. (2003). Surface wave methods: Acquisition, processing and inversion, *Ph.D. Thesis*, Politecnico di Torino, C Strobbia, Torino.

Tanimoto, T., S. Ishimaru, and C. Alvizuri (2006). Seasonality in particle motion of microseisms, *Geophys. J. Int.* **166,** no. 1, 253–266.

Yilmaz, O. (2001). *Seismic Data Analysis: Processing, Inversion, and Interpretation of Seismic Data, No. 10*, Investigations in Geophysics, Society of Exploration Geophysicists, Tulsa, Oklahoma.

Ying, Y., C. J. Bean, and P. D. Bromirski (2014). Propagation of microseisms from the deep ocean to land, *Geophys. Res. Lett.* **41,** no. 18, 6374–6379.

Seismology Lab
School of Geological Sciences
University College Dublin
Dublin, Ireland

Manuscript received 26 March 2016;
Published Online 17 May 2016